



Hierarchical Bi₂MoO₆ spheres in situ assembled by monolayer nanosheets toward photocatalytic selective oxidation of benzyl alcohol

Kaiqiang Jing^a, Wen Ma^b, Yahang Ren^a, Jinhua Xiong^a, Binbin Guo^{a,b}, Yujie Song^a, Shijing Liang^{a,*}, Ling Wu^{a,b,*}

^a State Key Laboratory of Photocatalysis on Energy and Environment, Fuzhou University, Fuzhou, 350116, PR China

^b State Key Laboratory of Structural Chemistry, Fujian Institute of Research on the Structure of Matter, Chinese Academy of Sciences, Fuzhou, Fujian, 350002, PR China

ARTICLE INFO

Keywords:

Monolayer nanosheets
Oxygen vacancies
Surface coordination and activation
Photocatalysis
Benzyl alcohol

ABSTRACT

Hierarchical Bi₂MoO₆ spheres in situ assembled by monolayer nanosheets were successfully prepared via a cetyltrimethylammonium bromide (CTAB)-assisted assembled strategy under different prepared conditions. The structure, morphology and surface chemical state of the prepared samples were well characterized. The AFM images (Atomic force microscopy) present that the average thickness of the nanosheets for two typical samples are about 0.81 and 0.84 nm, respectively. The analysis results of O 1s XPS and in-situ ESR indicate that there are different concentration oxygen vacancies (OVs) in two prepared samples (denoted as Vo-rich and Vo-poor). Time-resolved fluorescence emission decay spectra show that the carriers lifetime of Vo-rich and Vo-poor are 5.18 and 1.59 ns, respectively. Moreover, in-situ FTIR of benzyl alcohol (BA) absorption results suggest that rich oxygen vacancies could facilitate BA coordination. Vo-rich and Vo-poor present 38.2% and 7.1% of conversion with high selectivity for benzyl alcohol oxidation under visible light irradiation, respectively. The higher performance for Vo-rich was attributed to rich oxygen vacancies which act as the sites for the reactant activation. Finally, a feasible reaction mechanism was proposed to elucidate that enhanced photocatalytic activity over the Vo-rich.

1. Introduction

Over the past decades, photocatalysis with clean, high-efficiency and non-extra pollution merits has aroused extensive attention in clean energy, environmental remediation and fine chemical synthesis [1–6]. Recently, it has been expanding to the aspect of green, high-efficiency organic synthesis. Numerous photocatalysts with special morphologies and structure have been developed for organic synthesis such as metal oxide (TiO₂ [7–10], Nb₂O₅ [11]), titanate nanosheets [12–14], polymeric graphitic carbon nitride (g-C₃N₄ [15–17]), metal organic frameworks (MOFs), [18–22] layered double hydroxides (LDHS) [23,24]. Traditionally, most of researchers focus on the separation of photo-electron-hole pairs, regulating the band structures and basic photocatalytic elements, while concentrate less on the surface coordination and activation with reactants as well as defects in the field of organic synthesis. Therefore, to explore suitable photocatalytic materials holds great promise to make best understand of photocatalytic process. However, most layered materials suffer from low selectivity and conversion in organic reaction due to high rate recombination of photo-generated charges and the fact that there are relatively few surface

active sites [25]. Two-dimensional (2D) nanosheets have sparked considerable interests owing to their distinctive characteristics, such as several-nanometer thickness, large surface areas, abundant active sites, ultrafast charge separation and large fraction of unsaturated surface sites [26–29], that give them enhanced performance in organic synthesis.

Among these photocatalytic materials, Bi₂MoO₆, one of the simplest Aurivillius-type compounds, constructed by alternating layer between (Bi₂O₂)²⁺ and (MoO₄)²⁻, has shown promising prospect for photocatalytic organic synthesis [30,31]. Many researchers have made great efforts to improve photocatalytic performances over Bi₂MoO₆, such as noble metal loading, heterojunction fabrication and so on [32,33]. Very recently, our research group reported a cetyltrimethylammonium bromide (CTAB)-assisted bottom-up method to synthesize the monolayer Bi₂MoO₆ nanosheets for selective oxidation benzyl alcohol [34], which showed superior photocatalytic performance in comparison of bulk counterpart. It can improve the BET surface area of the prepared samples if monolayer nanosheets are further assembled into hierarchical microspheres, thus contributing to adsorbing more reactants. Moreover, introducing different concentration of oxygen vacancies into

* Corresponding authors at: State Key Laboratory of Photocatalysis on Energy and Environment, Fuzhou University, Fuzhou, 350116, PR China.

E-mail addresses: sjliang2011@gmail.com (S. Liang), wuling@fzu.edu.cn (L. Wu).

<https://doi.org/10.1016/j.apcatb.2018.10.027>

Received 11 July 2018; Received in revised form 26 September 2018; Accepted 10 October 2018

Available online 11 October 2018

0926-3373/ © 2018 Elsevier B.V. All rights reserved.

monolayers may extend the light adsorption towards longer wavelength, accounting for improving photocatalytic activity. Therefore, it may be still valuable for preparing Bi_2MoO_6 with hierarchical architecture and revealing their surface characters. Herein, we develop a cetyltrimethylammonium bromide (CTAB)-assisted method to synthesize the hierarchical Bi_2MoO_6 via assembling monolayer nanosheets with different concentration oxygen vacancies. The sample with rich oxygen vacancies shows 5.5 times higher activity than that with poor oxygen vacancies for photocatalytic selective oxidation of benzyl alcohol (BA) under visible light irradiation. The roles of oxygen vacancies and surface properties in monolayer nanosheets are revealed on the analytic results of XPS, in situ ESR and in situ molecular spectroscopic techniques. Based on in-situ FTIR results, it is inferred that the surface OV's would coordinate and activate BA. Moreover, the unique structure, large specific surface area, strong light absorption and improved carrier lifetime were investigated by TEM, AFM, BET, UV-vis DRS and Time-resolved fluorescence emission decay spectra. The structure features of hierarchical spheres with large pore volume would facilitate reactive species to interact sufficiently. It is hoped that the present study might provide a feasible method to fabricate hierarchical sphere assembled by monolayer nanosheets with different concentration oxygen vacancies and understand the reaction pathway between defects and reactants at a molecular level [35,36].

2. Material and method

2.1. Reagents and chemicals

The following materials and reagents were used as starting materials: Bismuth nitrate pentahydrate ($\text{Bi}(\text{NO}_3)_3 \cdot 5\text{H}_2\text{O}$, A.R., Sinopharm Chemical Reagent Co. (SCRC)), Hexadecyltrimethyl ammonium bromide ($\text{C}_{19}\text{H}_{42}\text{BrN}$, SCRC), Sodium molybdate dehydrate ($\text{Na}_2\text{MoO}_4 \cdot 2\text{H}_2\text{O}$, A.R., SCRC), Ethylene glycol ($\text{C}_2\text{H}_6\text{O}_2$, SCRC), ethanol (EtOH, SCRC), deionized water.

2.2. Preparation of hierarchical Bi_2MoO_6 spheres

The hierarchical Bi_2MoO_6 spheres were synthesized by a one-pot solvothermal process. 0.970 g of $\text{Bi}(\text{NO}_3)_3 \cdot 5\text{H}_2\text{O}$ and 0.3 g of CTAB were added into 60 ml of ethylene glycol. After vigorous stirring for 30 min, 0.242 g of $\text{Na}_2\text{MoO}_4 \cdot 2\text{H}_2\text{O}$ was put into the reacted system and the mixture was then transferred into a 100 mL Teflon-lined stainless steel autoclave. The autoclaves were put in an oven and solvothermally treated at different temperature and time. After they were cooled to the room temperature, the yellow products were centrifuged and washed by ethanol and deionized water for many times. Finally, the prepared samples were dried at 60 °C in a vacuum oven. The samples prepared at 180 °C for 3 h and 120 °C for 12 h were labeled as Vo-rich and Vo-poor, respectively. For comparison, the Bi_2MoO_6 samples at 180 °C and at 120 °C with different solvothermal time such as 3 h, 6 h, 12 h and 16 h were also prepared by the same procedure except solvothermal temperature and time.

2.3. Materials characterization

The as-prepared samples were characterized by powder X-ray diffraction (XRD) on a Bruker D8 Advance X-ray diffractometer operated at 40 kV and 40 mA. Ultraviolet–visible diffuse reflectance (ultraviolet–visible diffuse reflectance spectrum) spectra were obtained with a self-supporting sample disk on an ultraviolet–visible spectrophotometer (Cary 500). BaSO_4 was used as a reflectance standard. X-ray photoelectron spectra (XPS) were acquired on an ESCALAB MKII with $\text{Mg K}\alpha$ ($h\nu = 1253.6$ eV) as the excitation source. The binding energies obtained in the XPS spectral analysis were corrected for specimens charging by referencing C 1s to 284.8 eV. The morphologies of the products were examined by field emission scanning electron

microscopy at an accelerating voltage of 5 kV (Hitachi New Generation SU8010). Transmission electron microscopy (TEM) images and higher-resolution transmission electron microscopy (HRTEM) images were recorded using a JEOL model JEM2010 EX microscope at an accelerating voltage of 200 kV. We conduct SEM and TEM to investigate the structure and morphology using the direct obtaining prepared samples. AFM images were recorded using Agilent 5500 AFM (Agilent Technologies, USA). All the images were acquired using tapping mode under ambient conditions (ca. 40–50 % relative humidity, 25 °C temperature). The used Si cantilevers/tips (Bruker) have a spring constant of 40 N m^{-1} and a resonance frequency of 300 kHz. During an AFM experiment, samples were dispersed in ethanol using an ultrasonic bath for 10 min and then the dispersion was diluted in ethanol. A drop of the above diluted dispersion was deposited on a new cleaved mica surface and dried in air used to evaluate the morphology of the obtained nanosheets on the mica substrate. The electrochemical analysis was carried out in a conventional three electrode cell using a Pt plate and an Ag/AgCl electrode as the counter electrode and reference electrode, respectively. The electrolyte was 0.2 M Na_2SO_4 aqueous solution without additive (pH 6.8). The working electrode was prepared on indium-tin oxide (FTO) glass that was cleaned by sonication in ethanol for 2 h and dried at 353 K. The boundary of FTO glass was protected using Scotch tape. The 5 mg of sample was dispersed in 0.5 mL of dimethyl formamide (DMF) by sonication to get slurry. The slurry was spread onto the pretreated FTO glass. After air drying, the working electrode was further dried at 393 K for 2 h to improve adhesion. Electron spin resonance (ESR) signals were recorded with a Bruker A300 spectrometer. A 300 W Xe lamp (Beijing Trustech, PLS-SXE300c) with a 400 nm cut-off filter was used as a light source. The Brunauer–Emmett–Teller (BET) surface area was measured with an ASAP2020 M apparatus (Micromeritics Instrument Corp). Raman spectra were collected via a multichannel modular triple Raman system (Renishaw Co.) with confocal microscope at room temperature using the 785 nm laser. The fluorescence life time spectra were recorded on a spectrophotometer (FLS980, Edinburgh Instruments Ltd.). Decay curves were analyzed at the emission of 490 nm for the Vo-rich under 377 nm excitation and at the emission of 470 nm for the Vo-poor under 377 nm excitation.

2.4. In-situ ESR (under vacuum conditions) measurement

Electron spin resonance (in-situ ESR) signals were recorded with a Bruker A300 spectrometer. 30 mg powder samples were pressed into a self-supporting in situ ESR quartz tube. Before the ESR measurements were initiated, the tube was treated under dynamic vacuum (2.7×10^{-3} Torr) to remove surface contaminants. The ESR spectra of the samples were recorded.

2.5. In-situ FTIR measurement

The In-situ infrared spectra of benzyl alcohol adsorbed on the catalysts were obtained on a NICOLET IS50 Fourier transform infrared (FT-IR) spectrometer at a resolution of 4 cm^{-1} . A total of 64 scans were performed to obtain each spectrum. Firstly, the powder samples were first pressed into a self-supporting IR disk (18 mm diameter, 20 mg), then the disk was placed into the sample holder which could be moved vertically along the cell's tube. Before initiating the FTIR measurements, the disk was treated under dynamic vacuum (2.7×10^{-3} Torr) at 300 °C for 2.0 h to remove surface contaminants. After the disk cooling to RT, 10 μL of benzyl alcohol was spiked into the cell with a syringe via the septum. 30 min later, after adsorption equilibrium was reached, the FTIR spectra of the samples were collected. The physisorbed benzyl alcohol was removed by a further evacuation at 100 °C for 15 min under 2.7×10^{-3} Torr, and then, another FTIR spectrum of the sample was then taken.

2.6. Photocatalytic activity test

Photocatalytic selective oxidation of benzyl alcohol was performed as follows. A mixture of alcohol (0.1 mmol) and 16 mg of catalyst was dissolved in the solvent of benzotrifluoride (BTF) (1.5 mL), which was saturated with pure molecular oxygen. The choice of solvent BTF is because of its inertness to oxidation and high solubility for molecular oxygen. Then the mixture was transferred into a 10 mL Pyrex glass bottle filled with molecular oxygen at a pressure of 1 bar and stirred to make the catalyst blend evenly in the solution. The suspensions were irradiated by a 300 W Xe arc lamp (PLS-SXE 300, Beijing Perfectlight Co. Ltd.) with a 400 nm-CUT filter to cut off UV light. After the reaction, the mixture was centrifuged to remove the catalyst particles completely. The remaining solution was analyzed with an Agilent Gas Chromatograph (GC-7890 N). Conversion of alcohol and selectivity for aldehyde were defined as follows:

$$\text{Conversion (\%)} = [(C_0 - C_{\text{alcohol}})/C_0] \times 100$$

$$\text{Selectivity (\%)} = [C_{\text{aldehyde}} / (C_0 - C_{\text{alcohol}})] \times 100$$

Where C_0 is the initial concentration of alcohol, and C_{alcohol} and C_{aldehyde} are the concentrations of the substrate alcohol and the corresponding aldehyde, respectively.

3. Results and discussion

As shown in Fig. S1, the XRD patterns of the prepared samples are matched well with the published data (JCPDS No.21-0102, $a = 5.506 \text{ \AA}$, $b = 16.226 \text{ \AA}$, and $c = 5.487 \text{ \AA}$). The crystallinity of the Vo-poor is poor relatively. However, no other crystalline phase is observed. SEM images of

prepared samples are shown in Fig. 1 A–D, it is obviously seen that the prepared samples display hierarchical microspheres morphologies composing of plenty of nanosheets with several micron in size. Fig. 1B and D reveal that the Bi_2MoO_6 nanosheets are curly and thin. The morphologies were further confirmed by TEM (Fig. 2A and C). It can be seen that the prepared samples are hierarchical spheres morphologies and nanosheets are almost transparent. The HRTEM images (Fig. 2B and 2D) reveal that marked interplanar spacings of the (131) planes for

the nanosheets over Vo-rich and Vo-poor, respectively [37,38]. These characterization results indicate that the hierarchical Bi_2MoO_6 spheres assembled by nanosheets were prepared successfully. To validate the thickness of the nanosheets on the spheres, we perform the atomic force microscopy (AFM, Fig. 3A–D). It shows that the average thickness of Vo-poor is 0.81 nm, and the other sample named Vo-rich is 0.84 nm, which are consistent well with 0.84 nm thickness of monolayer Bi_2MoO_6 nanosheets [34], (Fig. S2) offering straightforward evidence for preparing monolayer nanosheets established hierarchical Bi_2MoO_6 architectures successfully.

To investigate the morphology evolution of the hierarchical architectures, we prepared a series of samples at 180 °C and 120 °C with different solvothermal time. As shown in Fig. S3 and S4, it is demonstrated that the formation of hierarchical architectures needs the appropriate temperature and time based on the change of morphology in different time. It indicates that the prepared samples at 180 °C for 3 h and 120 °C for 12 h show highest quality hierarchical architectures with ultrathin nanosheets. Therefore, the possible formation mechanism of hierarchical architectures constructed by monolayer nanosheets was depicted in Scheme 1. Initially, Bi^{3+} ion can combine with Br^- anion to form the Bi-Br complex through the electrostatic interaction. The Br-anion can more unite the hydrophobic chains of CTA^+ ions to impede the stacking monolayers. Then, tuning reaction temperature and time, the two hierarchical architectures assembled via monolayer Bi_2MoO_6 nanosheets are formed by the reaction of the Bi-Br complex with MoO_4^{2-} . Meanwhile, ethylene glycol with high viscosity could form stereo-hindrance more easily. This phenomenon may not only further keep monolayers from stacking, but also induce these dispersed nanosheets to assemble loose porous hierarchical architectures for reducing the surface free energy [39]. That is to say, CTAB and ethylene glycol might play synergistic roles in forming hierarchical Bi_2MoO_6 spheres in situ assembled by monolayer nanosheets.

X-ray photoelectron spectroscopy (XPS) was further carried out to confirm the chemical composition of the prepared samples. Fig. S5 depicts the survey of the prepared samples, which shows that both of samples include Bi, O, Mo and C elements. The C 1s peak in the spectrum of Vo-rich and Vo-poor derives from a trace amount of adventitious carbon. The Bi 4f, Mo 3d and O 1s XPS spectra of Vo-rich and

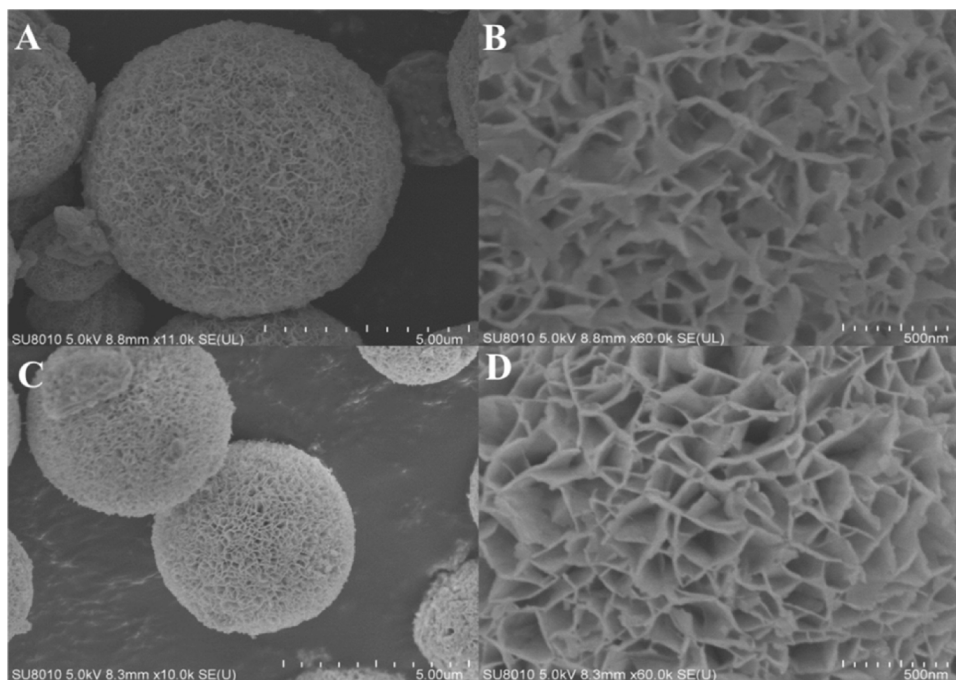


Fig. 1. SEM images of the prepared samples. (A–B) Vo-rich; (C–D) Vo-poor.

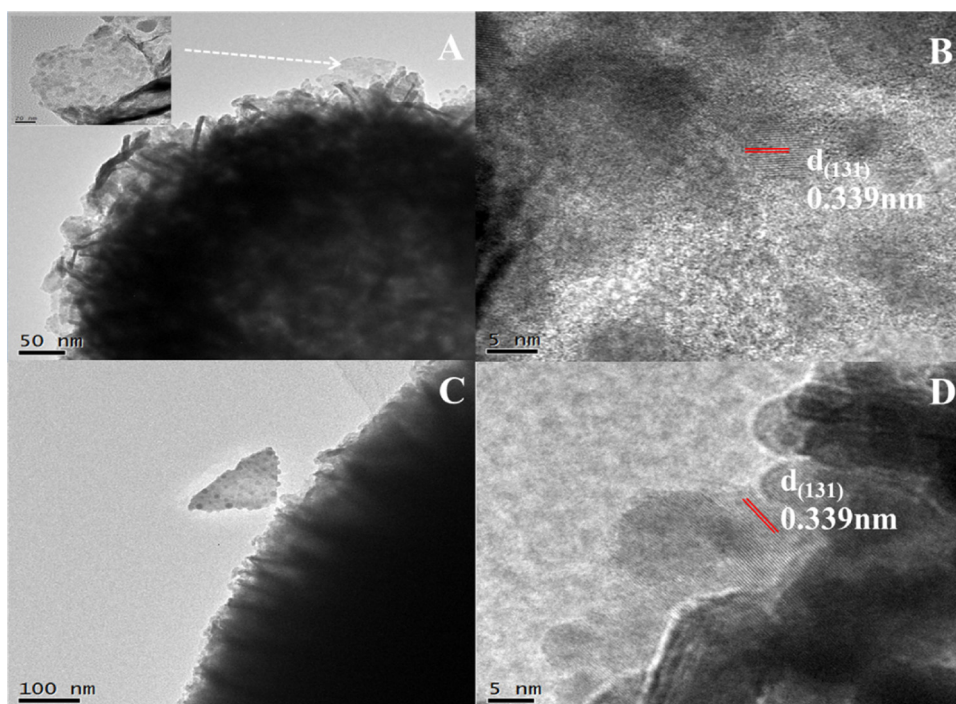


Fig. 2. TEM and HRTEM images of the prepared samples. (A–B) Vo-rich; (C–D) Vo-poor.

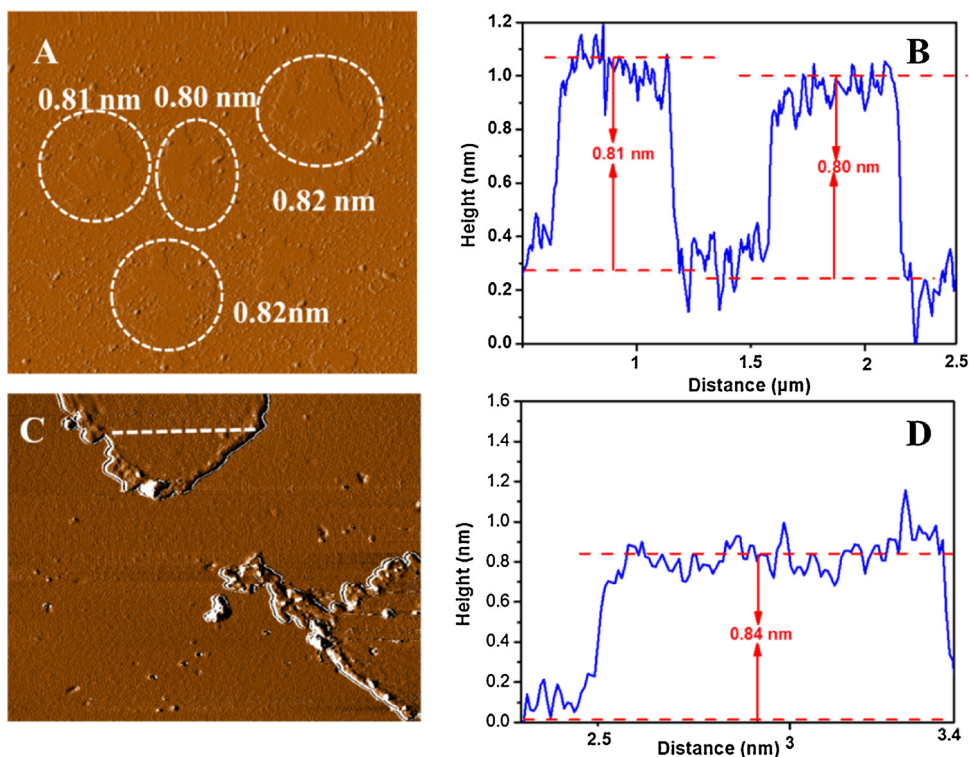
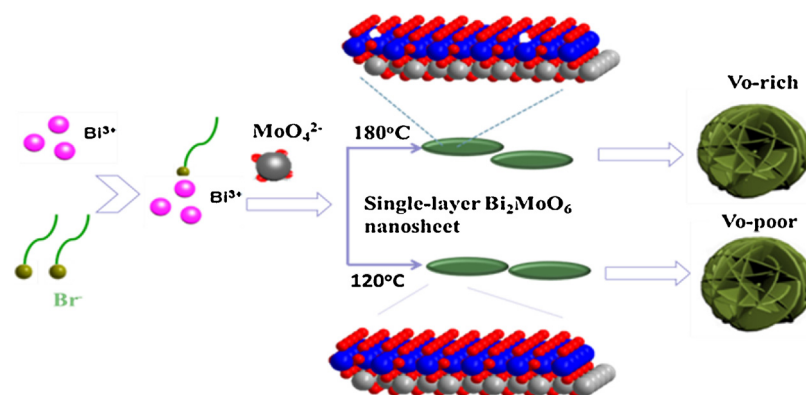


Fig. 3. AFM images of the prepared samples. (A–B) Vo-poor; (C–D) Vo-rich.

Vo-poor are shown in Fig. 4. The Bi 4f spectra (Fig. 4A) exhibit two contributions, $4f_{7/2}$ and $4f_{5/2}$ (resulting from spin–orbit splitting), located at 159.15 and 164.48 eV [40,41], respectively, which can be assigned to Bi^{3+} . Fig. 4C shows that the binding energies for the Mo $3d_{5/2}$ and Mo $3d_{3/2}$ of Mo^{6+} are around 232.3 and 235.4 eV [42], respectively. The O 1s spectra (Fig. 4B) clearly evidence the presence of two chemical environments for oxygen atoms. The peaks at around 529.8 eV for both samples are attributed to lattice oxygen, while the other one

located at 531.7 eV could be ascribed to oxygen vacancies (OVs) appeared in the spectrum of Vo-rich in contrast to the Vo-poor [43,44]. Meanwhile, as is shown in Table S1 in the Supporting Information, the position of O 1s at around 529.8 eV for both samples is attributed to lattice oxygen, which possesses almost same atom percentages. However, the estimated atom percentages (at. %) of oxygen vacancies for Vo-rich is 15.4%. It is higher than that of Vo-poor (10.4%), suggesting that reactive conditions with higher temperature and shorter time



Scheme 1. Diagram of hierarchical Bi_2MoO_6 architectures assembled from the monolayer nanosheets.

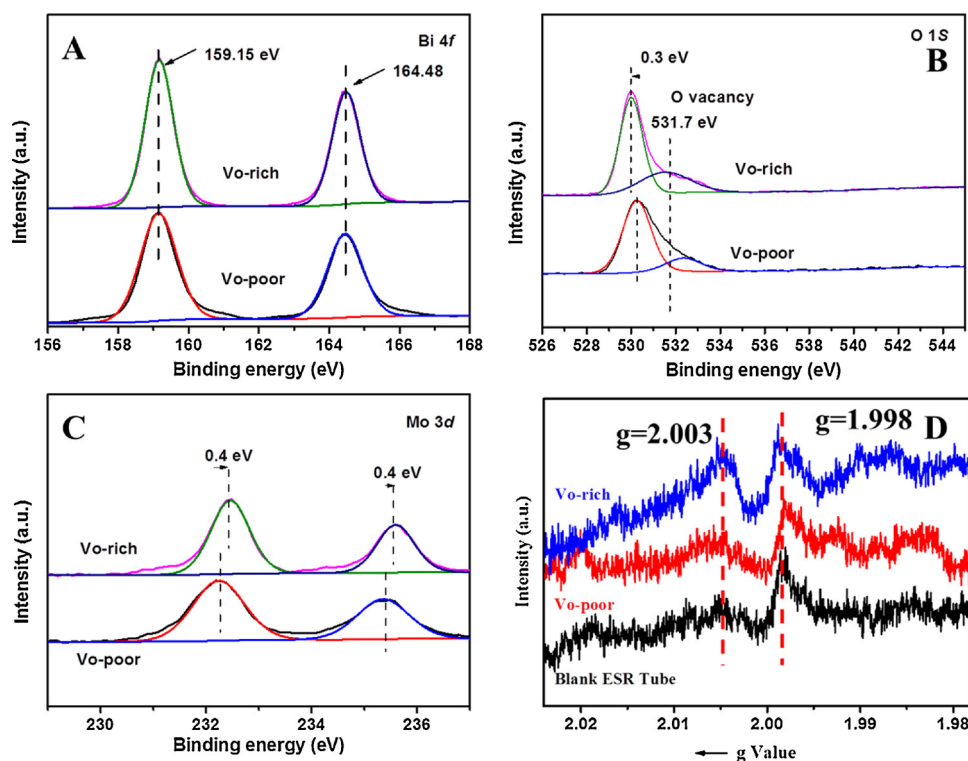


Fig. 4. High resolution XPS spectra of the prepared samples. (A) Bi 4f, (B) O 1s, (C) Mo 3d and (D) In-situ ESR spectra (under vacuum conditions).

might contribute to more OV. Besides, the results in Fig. 4B demonstrate that binding energy for O 1s in Vo-rich has shifted by 0.3 eV to a lower value compared to that in Vo-poor. Whereas Fig. 4C reveals that the binding energy for Mo 3d in Vo-rich has shifted by 0.4 eV to a higher value relative to Vo-poor. These shifts demonstrate that some electrons are transferred from Mo to O atoms in Vo-rich, implying that electrons in the Mo-O bonds are redistributed due to more OVs in Vo-rich. The oxygen vacancies were further manifested by in-situ ESR spectroscopy (Fig. 4D), which is a tool for examining unpaired electrons in materials. Vo-rich uniquely exhibits an intense ESR signal at $g = 2.003$, manifesting the electron trapping at oxygen vacancies [45]. It is worth noting that the ESR signal at $g = 1.998$ can be ascribed to the signal of blank tube when the ESR measurements were initiated under dynamic vacuum (2.7×10^{-3} Torr).

FT-IR spectra were further investigated to confirm whether CTAB on the surface of the Bi_2MoO_6 samples was completely removed and detect the surface species on the prepared samples. As shown in Fig. S6, characteristics of the C-H stretching mode at 2852 and 2922 cm^{-1} are not observed for both samples, indicating that the absence of residual

CTAB on the surface of the prepared samples [46]. The peaks at 730 and 765 cm^{-1} are ascribed to Mo-O stretching bands [47]. In contrast to Vo-poor, the Mo-O band of Vo-rich becomes sharper and shifts to low wavenumber, which may arise from the distortion of the Mo-O bond or the appearance of rich oxygen vacancies. Notably, the peak at around 1385 cm^{-1} attributed to vibration of O-H correspond to H_2O for Vo-poor shows higher intensity of signal compared to Vo-rich, suggesting there are more physical absorption H_2O on the surface of Vo-poor prepared via lower temperature. Therefore, physical absorption H_2O may occupy the oxygen vacancies and pore volume, resulting in poor photocatalytic performances.

Raman spectra were conducted to characterize the structure of the prepared samples. As shown in Fig. S7, the typical Raman band can be divided into main two ranges: $100\text{--}450 \text{ cm}^{-1}$ and $700\text{--}900 \text{ cm}^{-1}$, respectively. It is well known that the bands in the $100\text{--}450 \text{ cm}^{-1}$ region derives from the bending modes of the MoO_6 octahedra bonded with stretching and bending modes of the bismuth-oxygen polyhedra [48]. In the range of $700\text{--}900 \text{ cm}^{-1}$, the Raman modes mainly at 801 cm^{-1} (A_{1g} mode) and 850 cm^{-1} (A_{2u} mode) can be ascribed to the symmetric

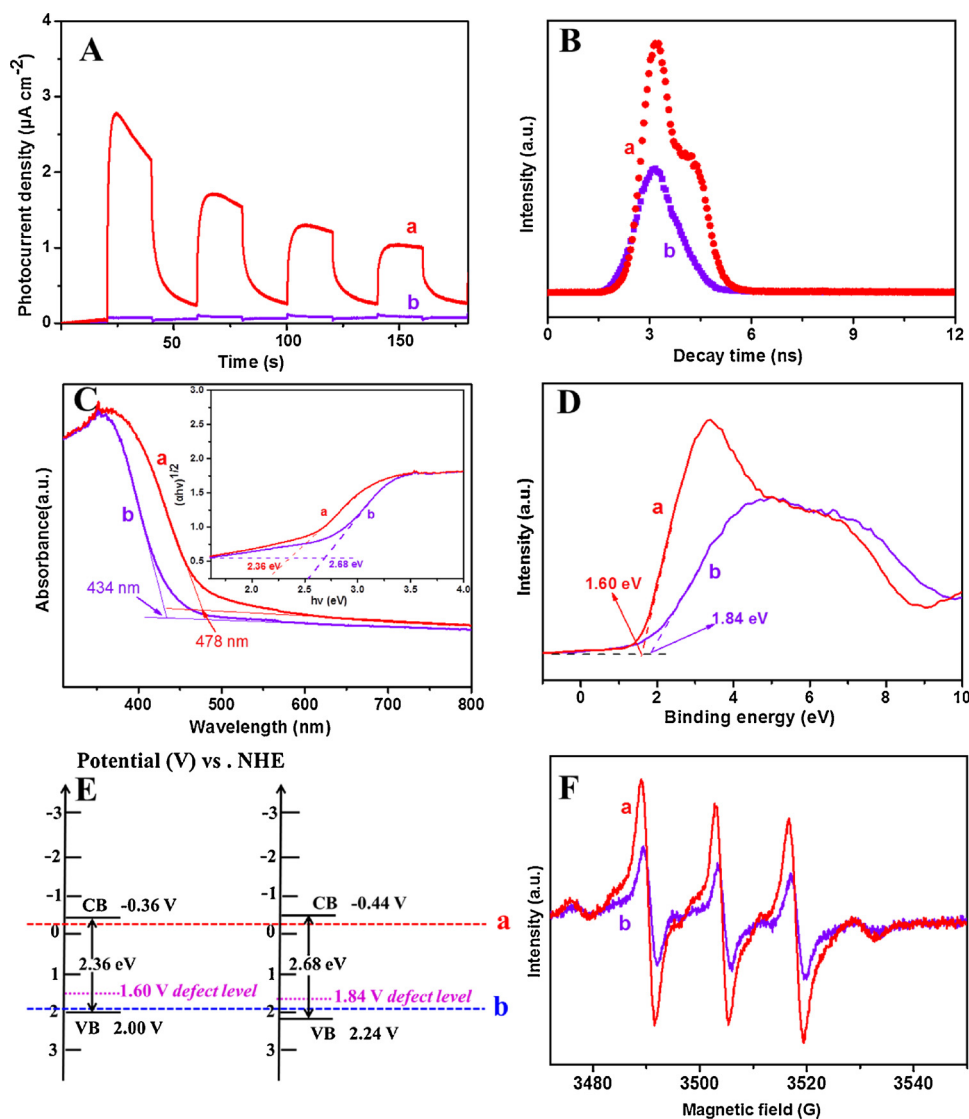


Fig. 5. Photoelectric characterizations for the prepared samples. (A) Photocurrent response. (B) Time-resolved fluorescence emission decay spectra. (C) UV-vis DRS spectra. (D) Valence band spectra. (E) Schematics the electronic band structures. (F) ESR spectra of superoxide radical species trapped by DMPO in Bi_2MoO_6 samples dispersion in the solvent of BTF under visible-light irradiation. a and b (in (A) - (D) and (F)) are defined as Vo-rich and Vo-poor. Dot line a and b in (E) are defined as ($\text{O}_2 + \text{e}^- \rightarrow \text{O}_2^-$, $E^\circ = -0.28 \text{ V}$ vs. NHE) and redox potential of benzyl alcohol oxidation ($+1.98 \text{ V}$), respectively.

and asymmetric stretching vibrations of the MoO_6 octahedra, which relate to motions of the apical oxygen atoms, located in vertical direction over layers [49]. Moreover, the mode at 716 cm^{-1} could be attributed to MoO_6 octahedra relating to the motion of the equatorial oxygen atoms within layers. For Vo-rich, it can be observed that the peaks at 796 and 839 cm^{-1} show broadening and slightly shifted toward low wavenumber, while the peaks at 716 cm^{-1} exhibits no evident shift and broaden in contrast to bulk Bi_2MoO_6 . This may result from the rearrangements of Mo–O in vertical direction and producing more oxygen vacancies [50,51]. However, the peak at 895 cm^{-1} correspond to Mo–O stretching modes for Vo-poor can be attributed to isolated MoO_4^{2-} tetrahedra. Besides, other peaks at 801 cm^{-1} and 850 cm^{-1} are not observed for Vo-poor. This results may indicate poor crystallinity for Vo-poor, which is consistent with the results of XRD pattern. Therefore, we may deduce that the Vo-rich has rich oxygen defects.

It is known that microstructure change may have a direct influence on BET surface area. Fig. S8 shows that the BET surface area of Vo-rich is calculated to be $48.1 \text{ m}^2 \text{ g}^{-1}$, which is almost 3.3 times larger than that of Vo-poor. Moreover, as shown in Table S2, it is clearly observed

that the pore volume of Vo-rich ($0.178 \text{ cm}^3/\text{g}$) is much higher than that of Vo-poor ($0.050 \text{ cm}^3/\text{g}$). The high surface area and pore volume may devote to the chemisorption and diffusion of more reactants.

The surface OV on the monolayer nanosheets provide more positive effect for the understanding of photocatalytic process. As we know, the surface OV could act as the trapping sites for photogenerated electrons, further accelerating the separation of charge carriers and the transportation of charge to reactants [52]. Electrochemical analysis and Time-resolved fluorescence emission decay spectra were carried out to confirm the separation rate of electron-hole pairs and photogenerated carrier lifetime. Photocurrent response (Fig. 5A) reveals that the response intensity in Vo-rich is almost 15 times than that in Vo-poor, demonstrating higher transformation and separation of photogenerated electron-hole pairs in Vo-rich. In addition, the time-resolved fluorescence emission decay spectra (Fig. 5B) show that respective average fluorescence lifetimes are 5.18 and 1.59 ns for Vo-rich and Vo-poor, respectively. These significantly increased carriers lifetime incontrovertibly indicate that OV on the monolayer nanosheets could facilitate the separation of photoinduced electron-hole pairs.

It is widely known that the surface OV can modify the optical

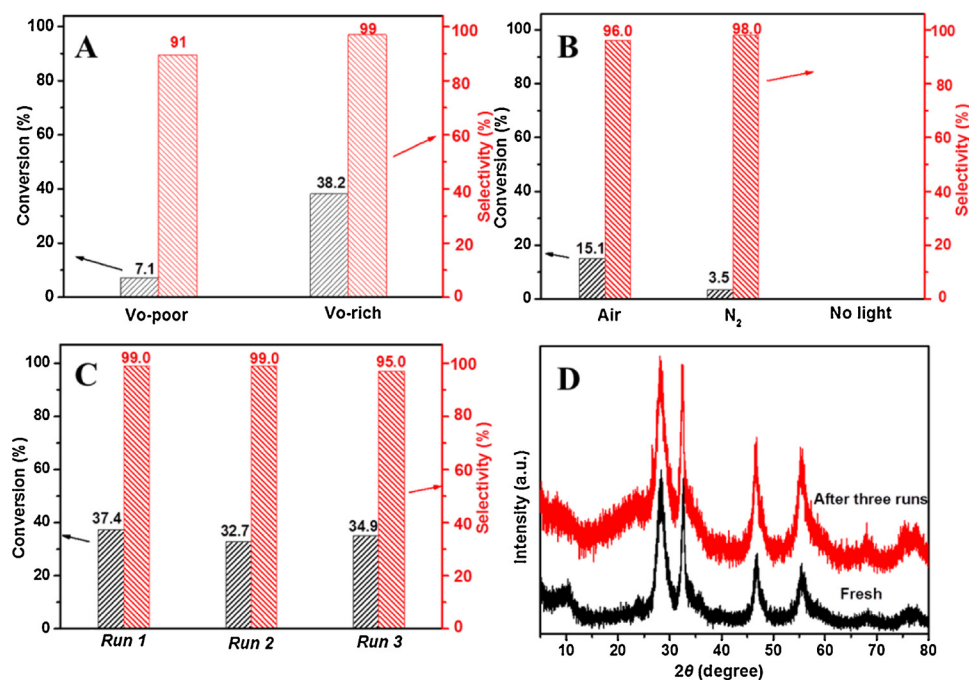


Fig. 6. (A) Photocatalytic selective oxidation of benzyl alcohol for the prepared samples. (B) Control experiment over Vo-rich. (C) Cyclic test of the photocatalytic oxidation of benzyl alcohol over Vo-rich. (D) XRD patterns of Vo-rich before the reaction and after three runs. Reaction condition: catalyst: 16 mg; $\lambda \geq 400$ nm at 298 K. Reaction time: 4 h.

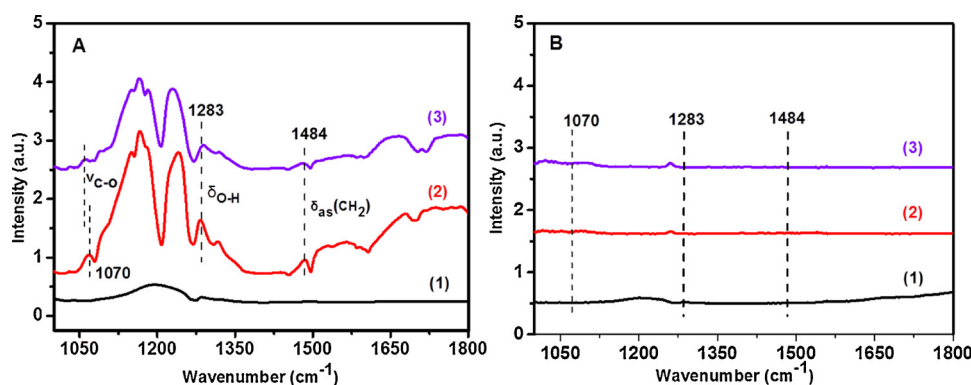


Fig. 7. In situ FTIR spectra of the prepared samples. (A) Vo-rich and (B) Vo-poor before and after the adsorption of and benzyl alcohol. Conditions: (1) after degassing at 300 °C for 2.0 h. (2) Adsorption for 30 min at RT (physisorption + chemisorption). (3) Further evacuation of the excess probe molecules at 100 °C for 15 min under 2.7×10^{-3} Torr (chemisorption).

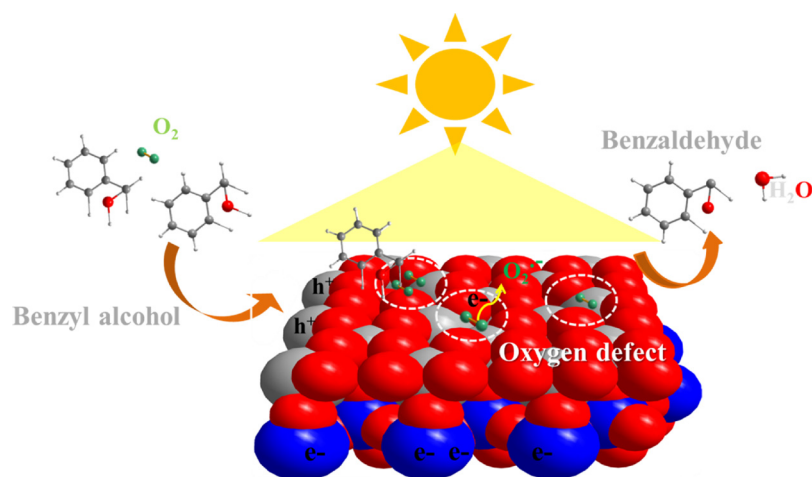


Fig. 8. Schematic illustration proposed feasible reaction mechanism for selective oxidation of alcohols to corresponding aldehydes over monolayer Bi₂MoO₆ nanosheets with oxygen vacancies under visible light illumination. Atoms are color labeled: Bi (white), Mo (blue), and O (red). (For interpretation of the references to colour in this figure legend, the reader is referred to the web version of this article.)

properties. OVs could extend the light adsorption towards longer wavelength, corresponding to narrower the band gap [53–56]. UV–vis DRS spectra (Fig. 5C) show that the absorption edges (λ_{abs}) of Vo-rich and Vo-poor are 478 nm and 434 nm, respectively. The Tauc plots (inset in Fig. 5C) reveal that the band gap energy of Vo-rich and Vo-poor are 2.36 eV and 2.68 eV. The Mott–Schottky plots (Fig. S9A–B) display the

flat-band potential of Vo-rich and Vo-poor are ca. -0.56 V and -0.64 V vs. Ag/AgCl at pH 6.8, respectively, corresponding to ca. -0.36 V and -0.44 V vs. NHE, respectively. This results reveal that the position of the conduction band (CB) over the two samples are more negative than the $O_2/O_2^{\cdot-}$ potential (-0.28 V vs. NHE), implying that both of them possess the ability of reducing oxygen to superoxide radicals (Fig. 5E).

According to the optical absorption spectra, the valence band (VB) of Vo-rich and Vo-poor would locate at about 2.00 V and 2.24 V. Intriguingly, it is found that valence band (VB) spectra (Fig. 5D) show the VB positions of Vo-rich and Vo-poor are 1.60 eV and 1.84 eV, more negative than the derived valence band values of Vo-rich and Vo-poor. This may be ascribed to the reason that more oxygen defects generate much localized states above the valence band edge, forming intermediate level [57,58]. It is demonstrated that superoxide radical species trapped by DMPO are observed in Fig. 5E and 5F. Moreover, Vo-rich can produce more superoxide radicals than Vo-poor. This is due to the fact that OV on the monolayer nanosheets can act as the active sites to trap O₂ molecular, contributing to enhancing photocatalytic oxidation organic reactions.

For photocatalytic selective oxidation benzyl alcohol (BA) to benzaldehyde under visible light irradiation ($\lambda \geq 400$ nm), Vo-rich shows 38.2% of conversion with 99% of selectivity, much higher than Vo-poor (7.1% of conversion with 91% of selectivity) in Fig. 6A. Furthermore, a set of control experiments demonstrate that O₂ and light are indispensable for oxidation BA in Fig. 6B. Besides, the influence of solvothermal temperature to photocatalytic performances is shown in Fig. S10, which demonstrates higher temperature may devote to high photocatalytic performances. Fig. 6C shows that there was no obvious loss in terms of the catalytic activity during three consecutive runs. Meanwhile, the XRD patterns (Fig. 6D) and TEM (Fig. S11) images suggest that morphology and crystal form for Vo-rich used by cyclic three runs are almost the same as the fresh Vo-rich, which further manifest by Raman spectra over Vo-rich before the reaction and after three runs, demonstrating that Vo-rich exhibits good stability and durability.

For comparison, we prepared time series samples at 180 °C. The XRD patterns (Fig. S13) show that the diffraction peaks of pure Bi₂MoO₆ prepared for 3 h and 6 h are perfectly indexed as the orthorhombic Bi₂MoO₆ (JCPDS Card No. 21-0102). However, the other (012) characteristic peaks of the rhombohedral phase Bi (JCPDS card no. 44-1246) centered at 27.1° can be clearly observed for the samples in 12 h and 16 h. This result may result in poor photocatalytic performance (Fig. S14), which could ascribe to the occupation of Bi over oxygen vacancies. Moreover, the photocatalytic performance over the samples prepared at 180 °C with the increase of time (Fig. S14) presents decrease gradually, which may attribute to the decrease of active sites and the occupation of Bi. This may provide an evidence that active sites locate on the monolayer nanosheets.

From Fig. 5E, we could find the valence band (VB) positions of Vo-rich and Vo-poor would locate at 1.60 and 1.84 eV, more negative than the redox potential of benzyl alcohol oxidation (+1.98 V) [59], indicating that both of the VB values could not directly drive this reaction from a thermodynamics point of view. Therefore, why the Vo-rich shows much higher photocatalytic performance than Vo-poor? We performed In situ FTIR spectroscopy over the prepared Bi₂MoO₆ samples. Fig. 7A and B reveals that Vo-rich exhibits a much stronger capacity of adsorbing BA compared with Vo-poor. Notably, Fig. 7A shows chemisorption of abundant BA on the surface of the Vo-rich. It is worthwhile mentioning that the characteristic peak of C–O

bond of BA is shifted to a lower wavenumber from physisorption + chemisorption to chemisorption on the surface of Vo-rich, demonstrating the rich OVs on the monolayer nanosheets could coordinate and activate BA.

Based on aforementioned viewpoint, a feasible reaction mechanism was proposed to elucidate the reaction process. The large surface area and pore volume on the monolayer nanosheets with rich OVs can contribute to interacting with the BA and oxygen. More importantly, as shown in Fig. 8, the oxygen vacancies on the monolayer nanosheets, as active sites, may play a synergistic role in photocatalytic oxidation organic reactions. OVs can coordinate and activate BA species, thus reducing the activation energy of BA. This may accelerate the photo-generated holes to oxidize BA,

which is the key step to oxidize BA. Besides, OVs serve as the centre of

electrons capturing and the adsorbed sites of oxygen, which may increase both the separation of photoinduced carriers and the capacity of oxygen activation. The superoxide radicals further react with the BA to accomplish the overall reaction. Therefore, the Vo-rich shows higher photocatalytic performance than Vo-poor due to possessing more OVs.

In summary, hierarchical Bi₂MoO₆ spheres in situ assembled by monolayer nanosheets with different concentration oxygen vacancies were synthesized successfully by adjusting temperature and time. Vo-rich shows that remarkable promotion for photocatalytic oxidation benzyl alcohol compared with Vo-poor, attributing to molecular thickness, large surface area, prolonged average lifetime of carries. More importantly, rich OVs could provide a platform not only for coordinating and activating BA, but also for trapping the photoexcited electrons and oxygen. These further accelerate the activation of BA and the separation of the photogenerated electrons and holes. This work may provide a general and efficient

strategy for fabricating hierarchical spheres assembled by monolayer nanosheets with different concentration oxygen vacancies and understanding the reaction pathway between defects and reactants.

Acknowledgements

This work was supported by the National Natural Science Foundation of China (21872032, 51672048 and 21677036) and the major science and technology projects of Fujian Province (2015YZ0001-1). S. Liang also thanks the Natural Science Foundation of Fujian Province for the Distinguished Young Scholar (2016J06004). Dedicated to Professor Jin-Shun Huang on the occasion of his 80th birthday.

Appendix A. Supplementary data

Supplementary material related to this article can be found, in the online version, at doi:<https://doi.org/10.1016/j.apcatb.2018.10.027>.

References

- [1] D.I. Enache, J.K. Edwards, P. Landon, B. Solsona-Espriu, A.F. Carley, A.A. Herzog, M. Watanabe, C.J. Kiely, D.W. Knight, G.J. Hutchings, *Science* 311 (2006) 362–365.
- [2] S. Fukuzumi, T. Kishi, H. Kotani, Y.-M. Lee, W. Nam, *Nat. Chem.* 3 (2011) 38–41.
- [3] R.A. Sheldon, I.W.C.E. Arends, G.-J.T. Brink, A. Dijkstra, *Acc. Chem. Res.* 35 (2002) 774–781.
- [4] T. Mallat, A. Baiker, *Chem. Rev.* 104 (2004) 3037–3058.
- [5] T. Ochiai, A. Fujishima, *J. Photochem. Photobiol. C* 13 (2012) 247–262.
- [6] Y. Qu, X. Duan, *Chem. Soc. Rev.* 42 (2013) 2568–2580.
- [7] S. Yurdakal, G. Palmisano, V. Lodo, V. Augugliaro, L. Palmisano, *J. Am. Chem. Soc.* 130 (2008) 1568–1569.
- [8] S. Higashimoto, N. Kitao, N. Yoshida, T. Sakura, M. Azuma, H. Ohue, Y. Sakata, *J. Catal.* 266 (2009) 279–285.
- [9] L. Yu, Y. Lin, D. Li, *Appl. Catal. B: Environ.* 216 (2017) 88–94.
- [10] X. Li, J.-L. Shi, H. Hao, X. Lang, *Appl. Catal. B: Environ.* 232 (2018) 260–267.
- [11] T. Shishido, T. Miyatake, K. Teramura, Y. Hitomi, H. Yamashita, T. Tanaka, *J. Phys. Chem. C* 113 (2009) 18713–18718.
- [12] Y. Song, H. Wang, X. Gao, Y. Feng, S. Liang, J. Bi, S. Lin, X. Fu, L. Wu, *ACS Catal.* 7 (2017) 8664–8674.
- [13] Y. Song, H. Wang, S. Liang, Y. Yu, L. Li, L. Wu, *J. Catal.* 361 (2018) 105–115.
- [14] H. Wang, Y. Song, J. Xiong, J. Bi, L. Li, Y. Yu, S. Liang, L. Wu, *Appl. Catal. B: Environ.* 224 (2018) 394–403.
- [15] S. Naya, K. Kimura, H. Tada, *ACS Catal.* 3 (2013) 10–13.
- [16] X. Lang, X. Chen, J. Zhao, *Chem. Soc. Rev.* 43 (2014) 473–486.
- [17] F. Su, S.C. Mathew, G. Lipner, X. Fu, M. Antonietti, S. Blechert, X. Wang, *J. Am. Chem. Soc.* 132 (2010) 16299–16301.
- [18] Y. Chen, Z. Wang, H. Wang, J. Lu, S. Yu, H. Jiang, *J. Am. Chem. Soc.* 139 (2017) 2035–2044.
- [19] R. Liang, L. Shen, F. Jing, W. Wu, N. Qin, R. Lin, L. Wu, *Appl. Catal. B: Environ.* 162 (2015) 245–251.
- [20] R. Liang, F. Jing, L. Shen, N. Qin, L. Wu, *Nano Res.* 8 (2015) 3237–3249.
- [21] L. Shen, R. Liang, L. Wu, *Chin. J. Catal.* 36 (2015) 2071–2088.
- [22] D. Wang, Y. Song, J. Cai, L. Wu, Z. Li, *New J. Chem.* 40 (2016) 9170–9175.
- [23] X. Yang, B. Chen, X. Li, L. Zheng, L. Wu, C. Tung, *Chem. Commun.* 50 (2014) 6664–6667.
- [24] Z. Wang, Y. Song, J. Zou, L. Li, Y. Yu, L. Wu, *Catal. Sci. Technol.* 8 (2018) 268–275.
- [25] B. Zhang, J. Li, Y. Gao, R. Chong, Z. Wang, L. Guo, X. Zhang, C. Li, *J. Catal.* 345 (2017) 96–103.

- [26] S.I. Shin, A. Go, I.Y. Kim, J.M. Lee, Y. Lee, S.-J. Hwang, *Energy Environ. Sci.* 6 (2013) 608–617.
- [27] Y. Zhou, Y. Zhang, M. Lin, J. Long, Z. Zhang, H. Lin, J.C. Wu, X. Wang, *Nat. Commun.* 6 (2015) 8340.
- [28] Y. Liu, J. Xiong, S. Luo, R. Liang, N. Qin, S. Liang, L. Wu, *Chem. Commun.* 51 (2015) 15125–15128.
- [29] H. Huang, R. Cao, S. Yu, K. Xu, W. Hao, Y. Wang, F. Dong, T. Zhang, Y. Zhang, *Appl. Catal. B: Environ.* 219 (2017) 526–537.
- [30] Y. Zhou, Z. Tian, Z. Zhao, Q. Liu, J. Kou, X. Chen, J. Gao, S. Yan, Z. Zou, *ACS Appl. Mater. Interfaces* 3 (2011) 3594–3601.
- [31] J. Bi, L. Wu, J. Li, Z. Li, X. Wang, X. Fu, *Acta Mater.* 55 (2007) 4699–4705.
- [32] S. Wang, X. Ding, X. Zhang, H. Pang, X. Hai, G. Zhan, W. Zhou, H. Song, L. Zhang, H. Chen, J. Ye, *Adv. Funct. Mater.* 27 (2017) 1703923.
- [33] J. Cai, J. Huang, Y. Lai, J. Mater. Chem. A 5 (2017) 16412–16421.
- [34] K. Jing, J. Xiong, N. Qin, Y. Song, L. Li, Y. Yu, S. Liang, L. Wu, *Chem. Commun.* 53 (2017) 8604–8607.
- [35] J. Xiong, L. Wen, F. Jiang, Y. Liu, S. Liang, L. Wu, *J. Mater. Chem. A* 3 (2015) 20627–20632.
- [36] S. Liang, L. Wen, S. Lin, J. Bi, P. Feng, X. Fu, L. Wu, *Angew. Chem. Int. Ed.* 53 (2014) 2951–2955.
- [37] X. Zhang, Z.H. Ai, F.L. Jia, L.Z. Zhang, *J. Phys. Chem. C* 112 (2008) 747–753.
- [38] J. Xiong, Y. Liu, D. Wang, S. Liang, W. Wu, L. Wu, *J. Mater. Chem. A* 3 (2015) 12631–12635.
- [39] S. Yuan, Y. Zhao, W. Chen, C. Wu, X. Wang, L. Zhang, Q. Wang, *ACS Appl. Mater. Interfaces* 9 (2017) 21781–21790.
- [40] H. Li, Q. Deng, J. Liu, W. Hou, N. Du, R. Zhang, X. Tao, *Catal. Sci. Technol.* 4 (2014) 1028.
- [41] Y. Xu, W. Zhang, *Dalton Trans.* 42 (2013) 1094–1101.
- [42] Z. Zhao, W. Zhang, Y. Sun, J. Yu, Y. Zhang, H. Wang, F. Dong, Z. Wu, *J. Phys. Chem. C* 120 (2016) 11889–11898.
- [43] H. Huang, K. Liu, K. Chen, Y. Zhang, Y. Zhang, S. Wang, *J. Phys. Chem. C* 118 (2014) 14379–14387.
- [44] S. Gao, Z. Sun, W. Liu, X. Jiao, X. Zu, Q. Hu, Y. Sun, T. Yao, W. Zhang, S. Wei, Y. Xie, *Nat. Commun.* 8 (2017) 14503.
- [45] Y. Zheng, T. Zhou, X. Zhao, W.K. Pang, H. Gao, S. Li, Z. Zhou, H. Liu, Z. Guo, *Adv. Mater.* 29 (2017) 1700396.
- [46] I. Luisetto, F. Pepe, E. Bemporad, *J. Nanopart. Res.* 10 (2008) 59–67.
- [47] H. Li, C. Liu, K. Li, H. Wang, *J. Mater. Sci.* 43 (2008) 7026–7034.
- [48] M. Maczka, J. Hanuza, W. Paraguassu, A.G. Souza Filho, P.T. Freire, C.J. Mendes Filho, *Appl. Phys. Lett.* 92 (2008) 112911.
- [49] M. Maczka, W. Paraguassu, A.G. Souza Filho, P.T.C. Freire, J. Mendes Filho, J. Hanuza, *Phys. Rev. B* 77 (2008) 094137.
- [50] L. Zhang, T. Xu, X. Zhao, Y. Zhu, *Appl. Catal. B: Environ.* 98 (2010) 138–146.
- [51] C. Kongmark, V. Martis, A. Rubbens, W. van Beek, *Chem. Commun.* (2009) 4850–4852.
- [52] H. Li, F. Qin, Z. Yang, X. Cui, J. Wang, L. Zhang, *J. Am. Chem. Soc.* 139 (2017) 3513–3521.
- [53] N. Zhang, X. Li, H. Ye, S. Chen, H. Ju, D. Liu, Y. Lin, W. Ye, C. Wang, Q. Xu, J. Zhu, L. Song, J. Jiang, Y. Xiong, *J. Am. Chem. Soc.* 138 (2016) 8928–8935.
- [54] S. Gao, B. Gu, X. Jiao, Y. Sun, X. Zu, F. Yang, W. Zhu, C. Wang, Z. Feng, B. Ye, Y. Xie, *J. Am. Chem. Soc.* 139 (2017) 3438–3445.
- [55] D. Cui, L. Wang, K. Xu, L. Ren, L. Wang, Y. Yu, Y. Du, W. Hao, *J. Mater. Chem. A* 6 (2018) 2193–2199.
- [56] Y. Lv, W. Yao, R. Zong, Y. Zhu, *Sci. Rep.* 6 (2016) 19347.
- [57] T. Su, Y. Yang, Y. Na, R. Fan, L. Li, L. Wei, B. Yang, W. Cao, *ACS Appl. Mater. Interfaces* 7 (2015) 3754–3763.
- [58] A. Naldoni, M. Allieta, S. Santangelo, M. Marelli, F. Fabbri, S. Cappelli, C.L. Bianchi, R. Psaro, V. Dal Santo, *J. Am. Chem. Soc.* 134 (2012) 7600–7603.
- [59] X. Xiao, J. Jiang, L. Zhang, *Appl. Catal. B: Environ.* 142–143 (2013) 487–493.